A Murine Delayed-Healing Model Associates Immune Response with Functional Bone Regeneration after Trauma

Matthew Patrick[1], Arnold Stromberg[2], Jaimo Ahn[3], Kurt Hankenson[3], and Ramkumar T. Annamalai[1]*

[1]Department of Biomedical Engineering, University at Buffalo, Buffalo, NY 14260
[2]Department of Statistics, University of Kentucky, Lexington, KY 40506
[3]Department of Orthopedic Surgery and Biomedical Engineering, University of Michigan, MI 48109

Author Correspondence:

Ramkumar T. Annamalai, PhD
328 Bonner Hall
University at Buffalo, NY 14260
Email: rtiruvan@buffalo.edu

Keywords: Hypertrophic Nonunion, Fracture, Interfragmentary strain, Delayed Healing, Biomarker

Abstract

Nonunion and delayed-union fractures pose a significant clinical challenge, often leading to prolonged morbidity and impaired quality of life. Fracture-induced hematoma and acute inflammation are crucial for establishing the healing cascade. However, aberrant inflammatory phenotypes can suppress healing and cause bone resorption. Elucidating these mechanisms is necessary to develop potent immunomodulatory therapies and prevent nonunion. Here, we report a delayed fracture healing model enabling the modulation of interfragmentary strain that mimics the etiology of hypertrophic nonunions to elucidate the role of dysregulated immune response in poor healing outcomes. High interfragmentary strain (>15%) was associated with larger callus volumes but delayed bone healing, increased inflammation, and inferior healing outcomes, while lower strain levels (<5%) corresponded to normal bone healing. In addition, we found distinct differences in the ossification, chondrification, and fibrosis patterns between high and low-strain groups, underscoring the significant impact of strain on the healing process. A comprehensive analysis of the systemic immune response revealed dynamic alterations in immune cell populations and factors, particularly within the early hours and days post-fracture. Several immune factors exhibited significant correlations with various functional healing outcomes, indicating their potential as predictive markers for assessing fracture healing progression. Our results also highlighted the significance of timely resolution of proinflammatory signals and the elevation of pro-regenerative immune cell phenotypes in promoting bone regeneration. Multivariate analysis revealed that CD25+ T-regulatory cells were influential in predicting proper bone healing, followed by CD206+ macrophages, underscoring the pivotal role of immune cell populations in the bone healing process. In conclusion, our study provides valuable insights into the intricate interplay between interfragmentary strain, immune response, and the ultimate outcomes of fracture healing. By shedding light on the underlying mechanisms that drive hypertrophic nonunion pathogenesis, our research lays the foundation for enhanced surgical management of nonunions and offers a promising avenue for developing targeted therapeutic interventions and personalized treatment strategies for individuals suffering from fracture nonunion.

1. Introduction

Nonunion of long bones is a debilitating injury, and treatment for such recalcitrant wounds is an urgent clinical need. In the US, an estimated 5-10% of the 8 million fractures occurring each year are associated with delayed union or nonunion[1]. A study of 832 long bone nonunions reported that this debilitating condition has devastating effects on the health-related quality of life, exceeding the impacts of stroke, type-1 diabetes, and AIDS[2]. Further, the distress caused by tibial and femoral-shaft nonunions was worse than congestive heart failure[3]. Currently, there is no standardized method for determining nonunions at early stages, and it takes at least 6-9 months to diagnose them conclusively[4]. The primary reason for this inadequacy is that the development of nonunion is not well understood, and predictive factors that promote healing and functional restoration are not well defined. Hence, there is an urgent need to bridge this gap through translational understanding to enhance the management of nonunion fractures.

Nonunion can be defined as the cessation of bone healing after a fracture. The FDA defines a nonunion as a fracture that has not healed for at least 9 months with no progressive signs of healing for 3 consecutive months[5]. The most widely accepted aseptic nonunion classification system developed by *Weber and Chec* identifies multiple differentiating characteristics[6]. With this, nonunion pathology can be simplified into fractures that lack specific biological cues, known as atrophic nonunion, and fractures that lack mechanical stability, known as hypertrophic nonunion[7, 8]. Atrophic nonunions can be identified through standard radiological imaging and are relatively less common clinically. However, hypertrophic nonunion resulting from mechanical instability is the most common pathology in the clinic, and its early conclusive diagnosis and treatment decision-making can be challenging. The animal models currently used to study nonunion are primarily atrophic[9]. These nonunion models do not represent the complex etiology of hypertrophic nonunions, which has led to our current lack of clinically translatable knowledge to diagnose and treat the majority of clinical cases. Hence, a clinically relevant hypertrophic nonunion model is needed to develop therapeutic and diagnostic strategies.

Early findings by *Wolff*[10], *Frost*[11], and *Perren*[12] on strain control and other biomechanical principles have laid the foundation for fracture-related surgical interventions. According to the strain theory, tolerance to local strain dictates the type of tissue developing in the fracture site. But determining the strains at the cellular level in the fracture site is challenging. However, simulations and models of tissue differentiation suggest that strains above 15% usually result in fibrous tissue formation, strains between 5% and 15% encourage endochondral ossification, and strains of <5% lead to direct bone formation[13]. As the fracture heals, the callus tissue gets stiffer over time due to cell invasion and ECM deposition and gradually minimizes the strain until it is conducive to ossification. However, in a hypertrophic nonunion, the strain is too high (>15%) to enable the initial granular tissue to progress to the next steps of healing and ossification. The high strain leads to chronic inflammation and a dysregulated immune response that further suppresses healing and causes bone resorption[14].

Recent studies show the dysregulated immune response, primarily due to altered leukocyte kinetics, as a major cause of poor prognosis of fractures in patients[15-18]. Systemic changes, including altered number or phenotype of inflammatory cells after severe trauma, can disrupt the inflammatory sequelae during bone regeneration. These changes are significantly different between patients with normal and impaired fracture healing in the early stages of injury (<2 weeks)[15]. Hence it has been hypothesized that peripheral immune biomarkers can distinguish fractures with a high probability of progressing into nonunion and enable physicians to intervene early. Furthermore, such biomarkers can significantly reduce time and morbidity associated with recalcitrant fractures. Efforts to elucidate these systemic differences in patients to use them as diagnostic biomarkers are gaining traction. But currently, no reliable biomarkers can prognose recalcitrant fractures that ultimately result in delayed union or nonunions.

Here we used a previously established blunt-trauma fracture model[19, 20] and modified it to create a delayed healing fracture model that replicates the pathophysiology of hypertrophic nonunion. Delayed-healing models were proposed previously[21] that withhold treatment after creating a segmental defect for an extended period, which does not mirror the clinical standard of care. To mirror the standard of care in the clinic, we stabilized the fractures using intramedullary fixation nails immediately and recreated the pathology of delayed healing by modulating the interfragmentary strain. We hypothesized that increasing the interfragmentary strain would result in poor bone healing, and this impairment can be associated with systemic immune dysregulation involving leukocyte kinetics and effector cytokines. To validate our murine model and test our hypothesis, we created femoral diaphyseal fractures and stabilized them with intramedullary nails that create varying strain. We quantified bone healing outcomes through bone morphometry, histology, and biomechanical tests. The intramedullary nails with reduced stiffness increased the interfragmentary strain (>15%) and delayed the bone healing outcomes. Fully stabilized fractures using stiffer nails reduced the interfragmentary strain (<5%) and represented uncomplicated bone healing. We also investigated the effects of fracture interfragmentary strains on the local and systemic immune response by measuring immune cell populations and biochemical factors using flow cytometry and multiplex assay, respectively. Then finally developed, univariate and multivariate models to delineate immune factors to predict functional healing. Our study not only offers a clinically relevant model for hypertrophic nonunions but also highlights the critical role of immune dysregulation in delayed bone healing, laying the groundwork for improved diagnostic and therapeutic approaches.

2. Methods

2.1. Animal model and surgical procedures

All animal procedures adhered to the guidelines approved by the Institutional Animal Care and Use Committee (IACUC) at the University of Kentucky. Adult male C5BL/6 mice (22-24 weeks old, The Jackson Laboratory) were used in this study. Prior to any procedures, animals underwent a minimum 7-day acclimatization period. The mice were randomly allocated into two experimental groups, comprising low and high-stiffness intermediary nails (n = 7/group). The intermediary nails were custom-manufactured from nitinol rods (Chamfr), with diameters ranging from 0.31 to 0.51 mm.

A well-established transverse fracture model, as previously described[20], was employed to create a femoral fractures. This method does not require any incisions of the muscles and mimics the fracture resulting from blunt trauma in humans with reproducible precision[22, 23]. Briefly, mice were anesthetized (1.5 mg of ketamine/kg + 1.5 mg of xylazine/kg body mass of mice), a bland ophthalmic ointment was applied, and the surgical site was shaved and wiped with 70% ethanol, followed by 10% povidone-iodine solution. A small incision was made at the patella and laterally dislocated to expose the knee joint. Using a 0.5 mm centering bit, a hole was made in the intercondylar notch, and an intramedullary guide tube (NiTi, 0.2 mm diameter) was inserted into the femur. With the guide tube in place, the right leg was positioned under the guillotine (blunt striker) of the murine fracture apparatus (RISystems). The blunt striker was then released to produce impact kinetic energy (E_k) of ~40 *mJ*, which is shown to create a transverse fracture in adult C57BL/6 mice[24]. The guide tube was then replaced with appropriate intermediary nails to stabilize the femur. The skin at the patella was sutured with 6-0 vicryl suture (Ethicon). Then, 1 mL of saline was administered intraperitoneally for hydration, followed by subcutaneous administration of buprenorphine SR (1.5 mg/kg body mass) for analgesia. The animals were then placed into a recovery cage and monitored as per the established post-operative animal care protocols. Animals were monitored daily for 7 days and weekly thereafter to ensure post-operative recovery.

2.2. Tissue collection and processing

Blood samples were also collected longitudinally from mice in K2 EDTA Microvette tubes (Sarstedt) from the submental and submandibular veins, following an alternating schedule. Baseline samples were obtained five days prior to surgery, with subsequent samples taken at 1 hour, 1, 3-, 7-, 14-, and 21-days post-surgery. Blood samples were centrifuged at 900 g for 5 minutes to separate cells from plasma. The supernatant containing plasma was stored at -80°C until analyzed using a multiplex assay kit. The cellular fraction of the blood was then processed, stained, and analyzed using flow cytometry.

For analyzing callus tissue cell populations, the tissue was minced, digested in a 0.1% collagenase solution (MP Millitec) at 37°C for 2 hours, neutralized with Dulbecco's modified Eagle's media (DMEM, Gibco) containing 10% fetal bovine serum (FBS, Gibco), filtered through a 100 µm cell strainer, and centrifuged at 400 g for 5 minutes to remove the supernatant. The cell pellet was then was then processed, stained, and analyzed using flow cytometry.

At 21 days post-surgery, the animals were euthanized, and their femurs (fractured and contralateral control) were collected in Dulbecco's modified Eagle's media (DMEM). The bones were subjected to morphometric analysis and biomechanical testing at room temperature. For histological analyses, the samples were then fixed in 10% neutral buffered formalin (ThermoFisher Scientific) for 24 hours, stored in 10 mM PBS at 4°C, and analyzed as described below.

2.3. MicroCT and morphometric analysis

Fracture healing outcomes were assessed at week 3 post-surgery using microcomputed tomography (microCT), as described[25]. To prevent any interference from the intramedullary nails, they were meticulously removed before the scanning process. A 360° scan was performed using a high-resolution small animal imaging system SkyScan1276 microCT (Bruker, Billerica, MA) with a 1 mm Aluminium filter with the voltage set to 70 kV and image pixel size 20.32 µm. Images were then reconstructed (NRecon, Bruker) with smoothing (set to 3), ring artifact correction (set to 4), and beam hardening correction (set to 30%). In preparation for morphometric analysis, cylindrical phantoms with diameters of 2 mm and known bone mineral densities of 0.25 and 0.75 g/cm^3 were submerged in deionized water, scanned, and reconstructed using the same settings.

The cortical region of the bone was delineated using a five-level OTSU algorithm. The threshold values for each level were determined based on the contralateral femur. Level 3 was scrutinized against the raw grey scale images to ensure the accuracy of the threshold, and it was subsequently employed as the cutoff threshold for analyzing the cortical region of the fractured bone. A 5 mm section (± 2.5 mm from the fracture) at the fracture site was designated as the Volume of Interest (VOI), with the cortical bone being defined as the Region of Interest (ROI). The ROI was processed algorithmically within the CTan software by Bruker to ensure consistent and precise analysis of both the callus and cortical bone separately. An adaptive threshold (Mean-C) was applied to the callus region to accommodate variations in mineral density and ensure alignment with the raw grey scale images. Three-dimensional analyses were then carried out on the callus and cortical sections using these chosen thresholds. The CTvox software (Bruker) was utilized to construct three-dimensional volume-rendered images of the bone.

2.4. Mechanical testing

Biomechanical properties of the bone were evaluated via a three-point bending test, as described previously[26]. The fracture and contralateral femurs were weighed, and their dimensions were determined through digital analysis of microCT scans. The three-point bending tests were executed using a Universal Testing Machine (Instron) at a strain rate of 30 mm/min, with an 8 mm span length, all performed at room temperature. Comprehensive whole bone properties, encompassing parameters like

stiffness, maximum force, work-to-fracture, and post-yield displacement (PDY), were deduced from the stress-strain curve. Furthermore, tissue-level parameters such as elastic modulus, yield stress, and ultimate stress were computed employing beam theory equations as listed below.

$$E = \frac{KL^3}{48I}$$

$$s_u = \frac{F_u Lc}{4I}$$

$$s_y = \frac{F_y Lc}{4I}$$

Where E = elastic modulus, K = stiffness, L = span length, I = moment of inertia, s_u = ultimate stress, F_u = ultimate force, c = distance from centroid of cross-section to outer most point on the cross-section, s_y = yield stress, and F_y = yield force. To calculate the average area moment of inertia (MOI) essential for these equations, a 5 mm segment (within ± 2.5 mm from the fracture site) was chosen from the microCT scans as the Volume of Interest (VOI), and a two-dimensional analysis was carried out.

The stiffness of the nitinol intramedullary nails was also measured through a 3-point bend test performed at a strain rate of 10 mm/min with an 8 mm span length. Stiffness was calculated from the slope of the linear region. The flexure strain of the stabilized femur was utilized as a metric for measuring the interfragmentary movement. It was computed under physiological loading conditions by employing the standard three-point flexure testing. The calculation for flexure strain in cylindrical geometries was as follows:

$$Flexture\ Strain = \frac{6Dd}{L^2}$$

Where D = axial displacement, d = cylinder diameter, and L = span length.

2.5 Histology

For histological examination, mice designated for this purpose were euthanized on day 21 post-surgery. Subsequently, the femurs with fractures were meticulously dissected and stripped of adjacent muscle tissues. The collected femurs then underwent decalcification using a solution containing 10% EDTA 4Na $2H_20$ (Sigma ED4SS) and 9% EDTA 2Na $2H_20$ (Sigma E5134) in sterilized deionized water. This decalcification solution was changed every three days over the course of three weeks. Following successful decalcification, the samples were paraffin-embedded and sectioned into 5 µm thick slices, which were subsequently mounted onto microscope slides (Apex Bond, Leica). The prepared slides were then subjected to staining using either a Movat's Pentachrome kit (StatLab) or a Picro-Sirius Red staining kit (StatLab), following the respective manufacturer's instructions or immunohistochemistry (IHC) as described previously.

Briefly, IHC was performed using the Ventana Discovery Ultra platform. 5 µm thick sections of formalin-fixed paraffin-embedded (FFPE) tissue were deparaffinized onboard, followed by on-board antigen retrieval as detailed below, primary antibody incubation at 37°C for 1 hour, detection as indicated below, and visualization with Ventana ChromoMap DAB.

SOX9 (cell signaling 82630 at 1:200) and SP7 (Thermo PA5-115697 at 1:100) were retrieved using Ventana CC1 buffer under standard conditions. Primary antibody was amplified by incubation with Ventana anti-rabbit-HQ, then anti-HQ-HRP for 20 minutes each. CD-31 (cell signaling 77699 at 1:100) was retrieved using Ventana CC2 standard with primary amplification and detection as above. SMA (Abcam ab5694 at 1:500) used CC1 standard and detection of primary antibody by Ventana

OmniMap anti-rabbit-HRP. All slides were run concurrently with known positive control tissue to confirm assay performance.

Stained slides were then imaged on an Axioscan Z7 with pentachrome and IHC stained slides being imaged under bright field light and Picro-Sirius Red slides being imaged under both bright field and polarized light. The fibrotic area was measured using Zeis image analysis software. Only slides including the center section of the femur and fracture callus were used for analysis. The fibrotic tissue areas were manually selected with the area calculation tool and summed together to get the total fibrotic area per slide. Fibrotic areas were only counted if they were inside the fracture callus or within the fracture gap in the medullary canal.

2.6. Flow cytometry and multiplex assay

Blood samples were collected at specific time points and processed as described above. Briefly, plasma was separated through centrifugation, and red blood cells (RBC) were lysed from the remaining sample following the manufacturer's guidelines using 1X RBC lysis buffer (eBioscience). Subsequently, an equal volume of 1X PBS (Gibco) was added to the suspension, followed by centrifugation at 400 g for 5 minutes. The resulting cell pellet was suspended in a blocking solution consisting of FACS buffer (1X PBS with 5% fetal bovine serum (Gibco) and 0.1% sodium azide) along with anti-mouse CD16/32 (eBioscience) for 10 minutes at 4°C to block Fc receptors.

The cells were then stained with fluorescently conjugated anti-mouse antibodies in FACS buffer for 45 minutes in the dark at 4°C. The detailed information regarding the fluorescent conjugates, clones, dilution factors, and suppliers for these antibodies can be found in **Supplementary Table 1**. The cell identification markers are listed in **Supplementary Table 2.** Following the staining procedure, the solution was removed through centrifugation at 400 g for 5 minutes, and the cells were subsequently resuspended in fresh FACS buffer. The samples were promptly subjected to analysis using a BD FACSymphony A3, and the data were processed using FlowJo software. Fluorescence-minus-one (FMO) controls for each antibody were employed to establish negative gates, ensuring a noise level of less than 1%.

To investigate the presence of inflammatory proteins, cytokines, and chemokines in the blood samples, a 32-analyte Milliplex MAP Mouse Cytokine/Chemokine Panel (Millipore, MCYTMAG-70K-PX32) was utilized. Initially, the plasma was isolated as previously described and then diluted in accordance with the manufacturer's recommendations.

2.7. Univariate and multivariate analysis

We conducted a comprehensive multifaceted analysis to investigate the relationship between immune cell populations, biochemical factors in both blood and callus tissues, and healing outcomes through conventional linear regression. Additionally, we employed multivariate models including linear and logistic regression. This included partial least squares regression (PLSR) analysis, which incorporated weighted averages of cell populations, cytokines, chemokines, and healing outcomes to identify the most influential immune factors. We utilized predictive analytics software JMP-PRO for all analyses. PLSR created principal components (latent variables, LV) combining immune cells, factors, and healing measures, and we assessed their predictive power by correlating them with the immune factors. We considered quadratic terms and variable interactions to enhance the model fits and employed the NIPALS algorithm with a 7 KFOLD validation method for generating linear plots. Notably, we focused on the first two linear combinations to identify the most influential healing factors.

2.8. Statistics

All measurements were performed with a minimum of 5 replicates. Data are plotted as either means with error bars representing the standard deviation or median with error bars representing the interquartile range. The Pearson correlation coefficient (r) was used to evaluate the linear correlation between two variables and the t-distribution to evaluate the associated p-value. To ensure the reliability of statistical comparisons, we subjected all groups to tests for normality and equal variance, employing the Shapiro-Wilk and Brown-Forsythe tests, respectively. In cases where both conditions were met, we used Student's t-test for two independent groups. When normality was not met, we applied the Mann-Whitney Rank Sum Test, and if the equal variance test failed, a Welch's t-test was used. For the analysis of systemic markers over time, a 2-way repeated measures ANOVA was performed. All statistical tests were performed in JMP or GraphPad Prism. Differences with $p < 0.05$ were considered statistically significant.

3. Results

3.1. Tailoring interfragmentary strain through intramedullary nail stiffness.

To induce delayed healing of the femoral fracture, we engineered intramedullary (IM) nails with varying stiffness using hyperflexible nitinol alloy (NiTi, ~3-30 N/mm, Supplementary **Fig.S1**) that enabled us to control interfragmentary strain. From the results of 3-point flexure tests and subsequent analyses, we selected a low-stiffness nail (2.7±0.05 N/mm) enabling >15% bending strain and a high-stiffness nail (16.5±0.41 N/mm) permitting <5% bending strain in the fracture site under typical hindlimb loads. First, we reamed the femurs with 25 or 27-gauge hypodermic needles to establish a snug fit with the low- and high-stiffness IM nails, respectively (**Fig.1A**). Then we created transverse fractures, stabilized them with low and high-stiffness IM nails, and assessed their maximum strain and stability through 3-point bending tests. Notably, the results indicated a slight reduction in stiffness of the fractured femurs stabilized with the nails compared to the IM nail alone (**Fig. 1B**, low - 1.96 ± 0.41 N/mm and high - 13.21 ± 1.53 N/mm). Despite this reduction, the application of physiological loads (1.5 – 3 N for a 30-gram mouse) to the stabilized femurs led to bending strains of 15.1±1.4% and 3.3±1.4% for low and high-stiffness nails, respectively (**Fig.1C**).

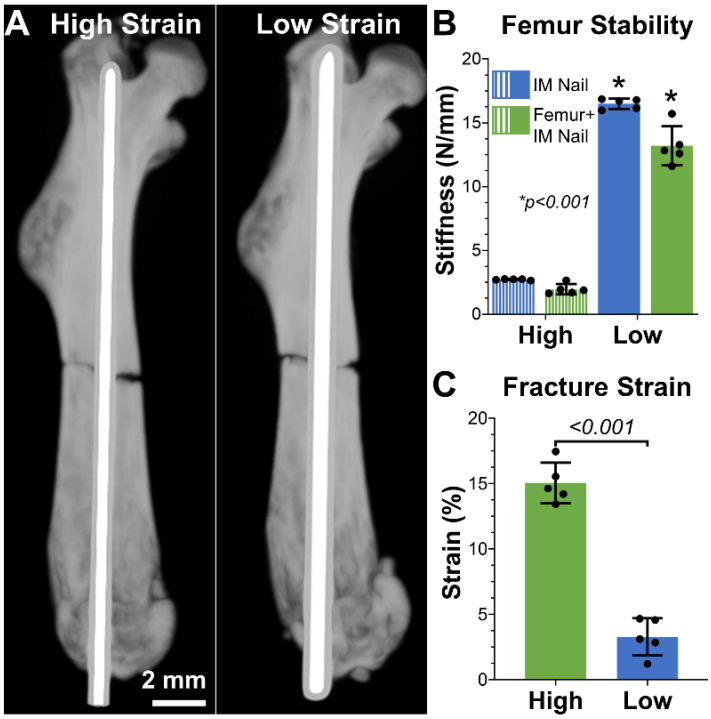

Figure 1. Stiffness of Intramedullary Nail Determines Interfragmentary Strain. A) *The maximum-intensity projection of microCT scans depicting fractured femurs stabilized with either low or high-stiffness IM nails.* ***B)*** *The graph presents a comparison of the stiffness of nitinol nails with those implanted into fractured femur phantoms (n = 5 per group).* ***C)*** *The flexure strain caused due to physiological loading on the stabilized femurs (n = 5 per group).*

3.2 Interfragmentary strain impacts fracture callus morphology.

Next, we investigated and compared the healing process in 22-week-old adult mice (n=12/group) with transverse fractures in the high and low-strain groups. At 3 weeks post-fracture, we retrieved the femurs, carefully removed the IM nails, and analyzed the bones using microCT (**Fig.2A-C**). The high-strain group developed larger calluses, while the low-strain group showed relatively smaller callus volumes. Morphometric analysis of the calluses revealed that the high-strain group had significantly higher callus tissue volume (TV, *p=0.003*, **Fig.2D**), callus bone volume (BV, *p<0.001*, **Fig.2E**), and mineral content (*p<0.001*, **Fig.2F**) compared to the low-strain group, mirroring observations in human patients[27]. However, no significant changes were observed in callus BV/TV or bone mineral density (BMD, **Fig.2G-H**).

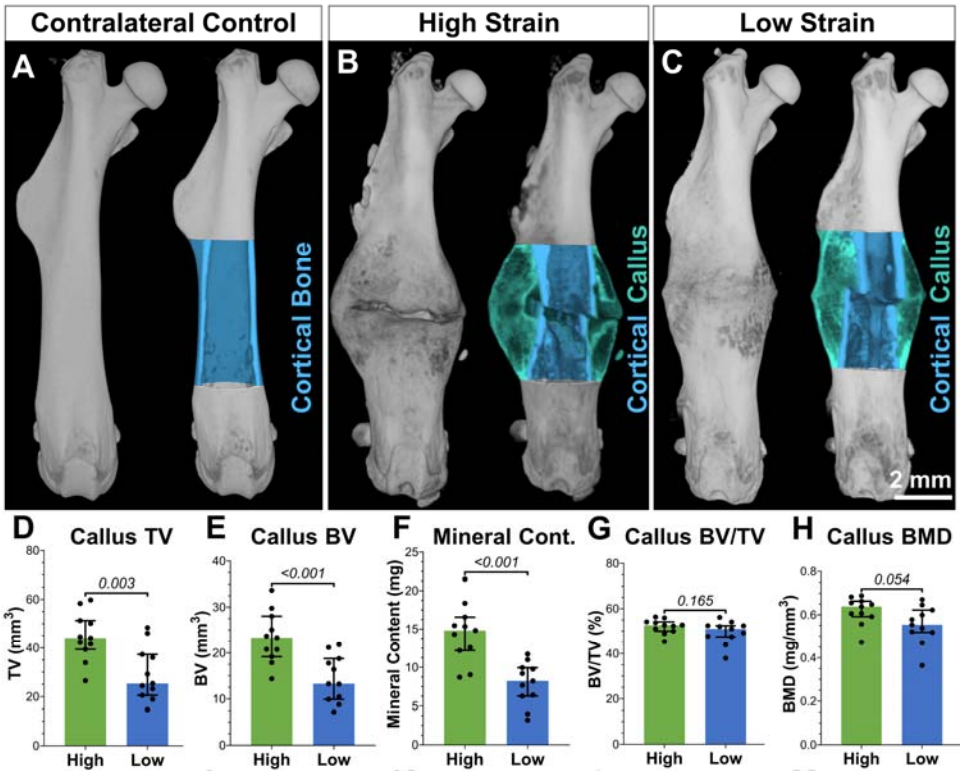

***Figure 2. Impact of interfragmentary strain on fracture healing outcomes at week 3**. (**A**) Representative 3D reconstructions of femurs from the control group. (**B**) High-strain group, and (**C**) Low-strain group at week 3 post-fracture with cross-sections of the fracture area (volume of interest). Light blue represents cortical bone, and teal denotes the callus tissue. (**D-F**) Comparative analysis of morphometric parameters of the fracture callus in the high and low-strain groups at week 3 (n=12/group).*

Table 1. Bone morphometric analysis. *The values presented are expressed as mean±SD. The sample size (n) for both groups is 11.*

Morphometric properties	High Strain	Low Strain	*p-value*
Callus TV (mm^3)	44.72 ± 9.9	29.47 ± 11.1	0.0028
Callus BV (mm^3)	23.31 ± 5.6	14.45 ± 5.1	0.0009

Callus Mineral content (mg)	14.45 ± 3.8	7.95 ± 2.8	0.0002
Callus BV/TV (%)	52.08 ± 3.2	49.45 ± 5.1	0.1652
Callus BMD (mg/mm^3)	0.62 ± 0.1	0.55 ± 0.1	0.0536
Callus Trabecular Thickness (mm)	0.115 ± 0.003	0.117 ± 0.004	0.2391
Callus Trabecular Number (mm^{-1})	4.51 ± 0.3	4.23 ± 0.5	0.140
Callus Trabecular Separation (mm)	0.16 ± 0.04	0.16 ± 0.1	0.8180
Callus Bone Surface (mm^2)	618.89 ± 140.6	384.03 ± 129.1	0.0006
Callus Bone Surface Density (mm^2/mm^3)	13.85 ± 0.7	12.98 ± 1.4	0.0902
Callus Specific bone surface (mm^2/mm^3)	26.61 ± 0.9	26.78 ± 1.1	0.6916
Callus Structure model index (SMI)	-0.69 ± 0.3	-0.26 ± 0.5	0.0204
Callus Connectivity density (mm^{-3})	196.87 ± 23.1	167.57 ± 29.5	0.0174
Callus Degree of anisotropy	1.25 ± 0.1	1.43 ± 0.2	0.0054

Pentachrome staining and immunohistochemistry were performed on week-3 femur sections from both the high-strain (**Fig. 3A**) and low-strain (**Fig. 3B**) groups, revealing notable differences in ossification, chondrification, vascularization, and fibrosis (**Fig. 3**). The high-strain group predominantly displayed larger and vascularized fibrotic calluses with reduced mucin-rich cartilaginous areas at week 3 (**Fig. 3A**(**i**), **B**(**i**)). Conversely, the low-strain group showed more matured woven bone with rich collagen deposition (**Fig.3A**(**ii**), **B**(**ii**)). The higher amounts of osteochondral bone formation in these regions were also confirmed using SOX9 (**Fig.3A**(**iii**), **B**(**iii**)) and SP7 (**Fig.3A**(**iv**) and **B**(**iv**)) immunohistochemistry indicating chondrocytes and osteoblasts, respectively. Further, the CD31/PECAM staining of the endothelial cells shows robust vascularization (**Fig.3A**(**v**) and **B**(**v**)) of the callus tissue in both groups, irrespective of the extent of ossification. Alpha-smooth muscle actin (ASMA) immunohistochemistry corroborated the presence of fibrotic areas in the high-strain callus tissues (**Fig. 3A**(**vi**). In contrast, ASMA staining was relatively minimal in the woven bone regions of the low-strain groups (**Fig. 3B**(**vi**)).

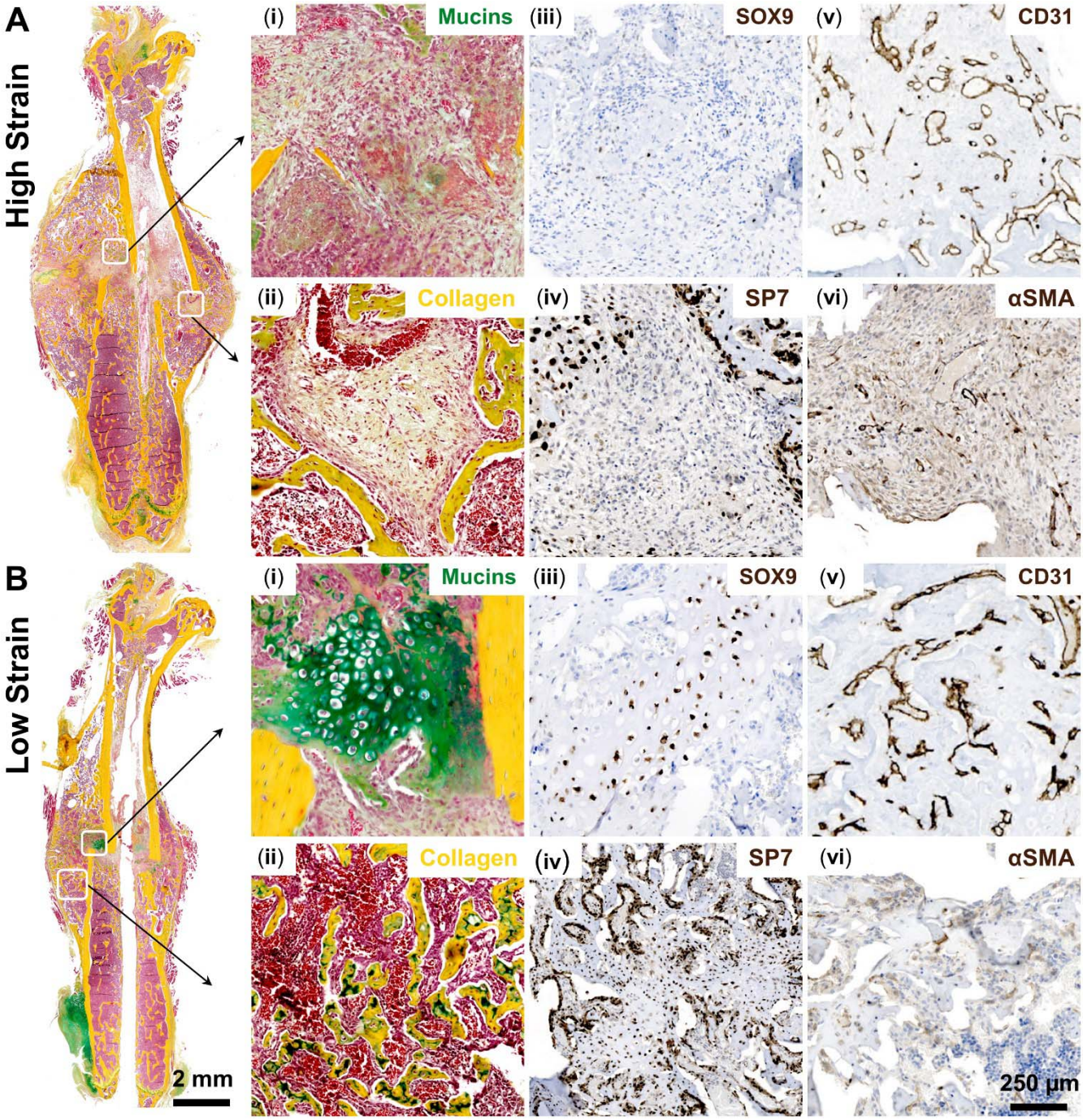

Figure 3. Interfragmentary strain impacts endochondral ossification. *Representative FFPE histological section of femurs from (**A**) high-strain group and (**B**) low-strain group retrieved at week-3 post-fracture and stained with pentachrome stain. Collagen fibers are stained yellow, mucins are stained blue, and fibrin and muscle are stained red. (i) and (ii) depict endochondral ossification. (iii) SOX9 staining confirming chondrification and (iv) SP7 staining confirming ossification.*

Picrosirius red staining and polarized light imaging showed a 2.9-fold increase (*p=0.0098*) in the area of fibrosis in the high-strain compared to the low-strain group (**Fig.5A-B**). Additionally, the

presence of fibrillar collagen deposition confirmed the fibrotic regions. Collectively, elevated interfragmentary strains resulted in callus tissue fibrosis and hindered functional healing, while lower-strain conditions supported greater ossification and promoted healthy bone healing.

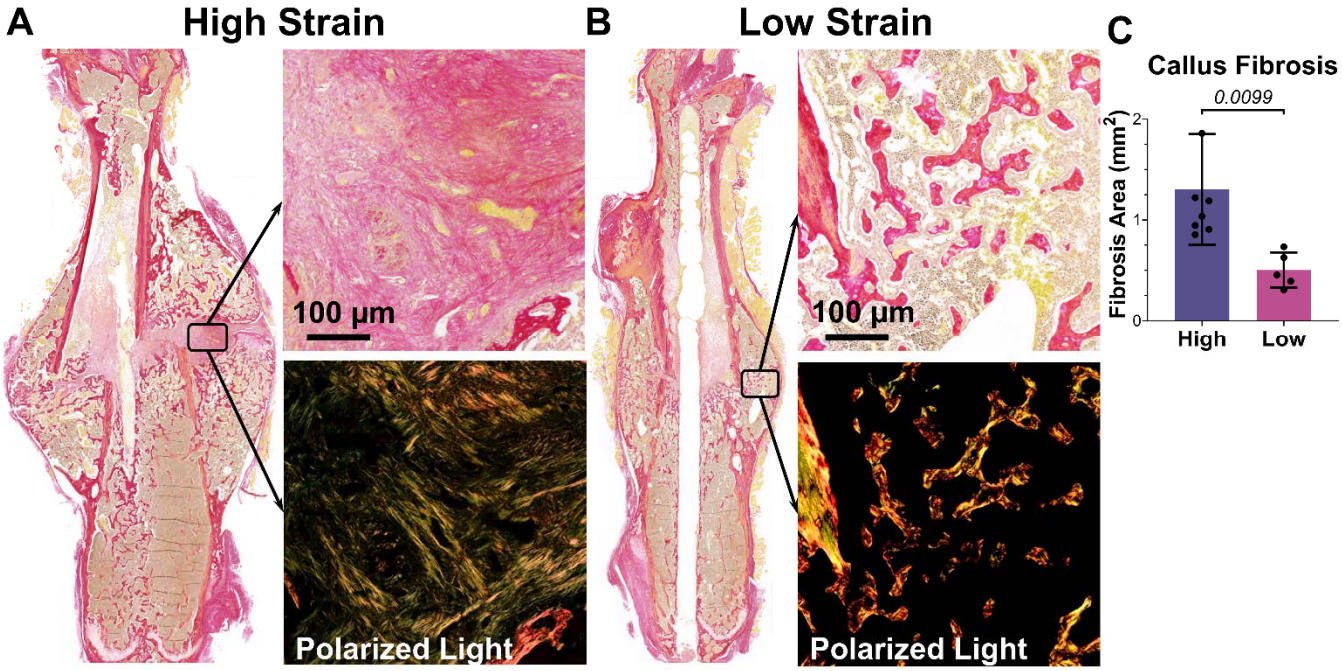

Figure 4. Higher interfragmentary strain leads to fibrosis. Picrosirius red staining reveals an increase presence of fibrotic callus regions in the (A) high-strain groups compared to the (B) low-strain group. (Bottom) Polarized light images of the callus validate the presence of fibrillar collagen in the high-strain group. (C) Quantitative assessment of the total fibrotic regions demonstrates the disparity between the two groups.

3.3 Interfragmentary strain impacts fracture healing outcomes.

To functionally evaluate the fracture healing, femurs from both low and high-strain groups were subjected to a 3-point bending test at week 3 post-fracture (n=12/group). This assessment encompassed whole-bone properties (stiffness, maximum force, force at yield, and post-yield displacement (PYD), **Fig.5A-D**) and tissue-level properties (work-to-fracture, elastic modulus, ultimate stress, and yield stress, **Fig.5E-H**) (see Table 2 for detailed values), following established methods[26].

Analysis of the test results revealed significant advantages in the low-strain group over the high-strain group in terms of stiffness (*p=0.024*, **Fig.5A**), maximum force (*p=0.036*, **Fig.5B**), ultimate stress (*p=0.002*, **Fig.5G**), and yield stress (p=0.032, **Fig.5H**). However, no significant differences were observed in force at yield, PYD, work-to-fracture, and elastic modulus between the groups (**Fig.5C-F**). Notably, the elastic modulus of the femurs in both groups strongly correlated with callus volume (R=0.87, *p<0.0001*). In summary, the comprehensive assessment of whole-bone and tissue-level properties highlights the reduced structural integrity and poorer healing outcomes in the high-strain group.

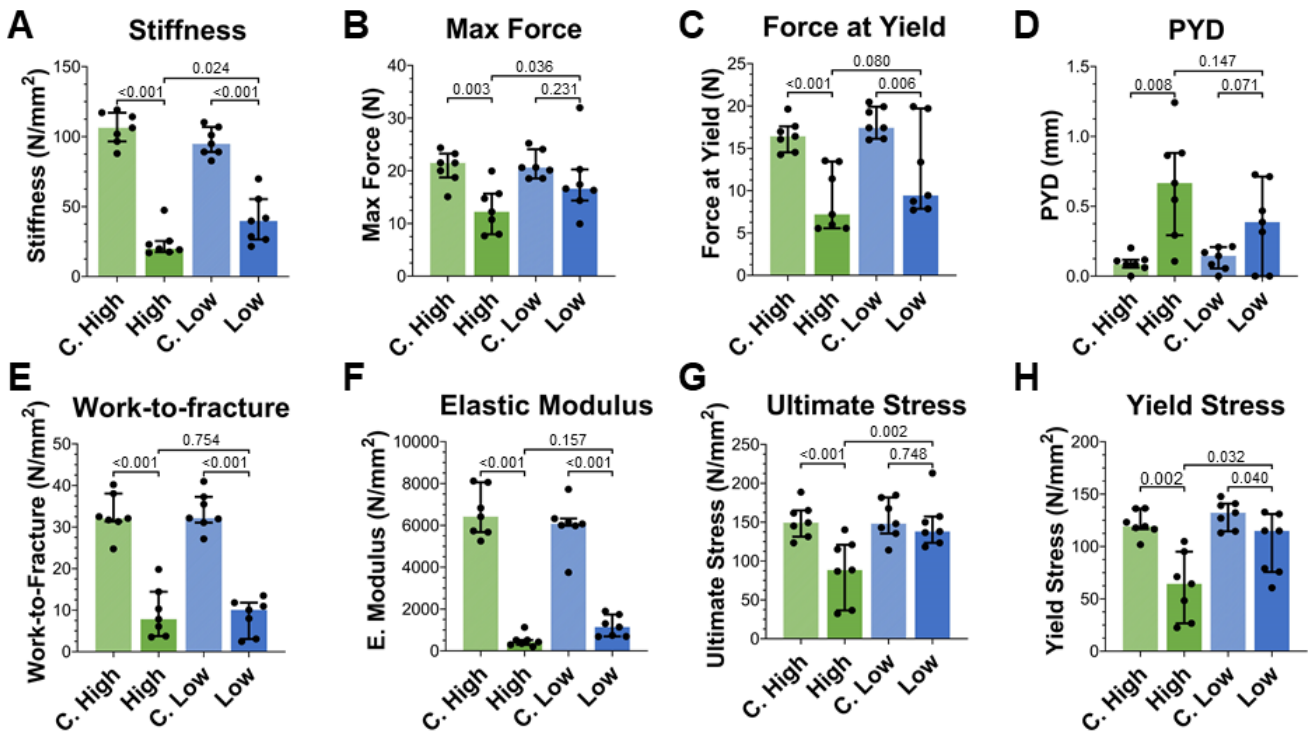

Figure 5. Impact of interfragmentary strain on fracture healing outcomes at week 3. *Three-point bending analysis of high and low-strain groups showing whole-bone (**A**) stiffness, (**B**) maximum force, (**C**) force at yield, and (**D**) post-yield displacement (PYD), and tissue-level properties (**E**) work-to-fracture, (**F**) elastic modulus, (**G**) ultimate stress, and (**H**) yield stress. Error bars depict medians with an interquartile range. n=7 per group. Contralateral control for high-strain and low-strain groups are denoted as C. High and C. Low, respectively.*

Table 2. Assessment of fracture healing outcomes*. Comparative evaluation of whole-bone and tissue-level mechanical properties of femurs subjected to 3-point bending testing. Values are presented as mean±SD. n = 7 for both groups.*

Mechanical properties	**Control High strain**	**High Strain**	**Control Low Strain**	**Low Strain**	***High vs Low p-value***	***C. High vs High p-value***	***C. Low vs Low p-value***
Stiffness (N/mm)	106.16 ± 11.5	24.17 ± 10.7	96.26 ± 10.2	40.48 ± 17.2	0.024*	<0.001*	<0.001*
Max load (N)	20.64 ± 3.1	12.72 ± 4.4	21.11 ± 2.6	18.19 ± 6.9	0.036*	0.003*	0.231
Force at Yield (N)	16.49 ± 1.8	8.95 ± 3.7	18.08 ± 1.8	12.39 ± 5.4	0.080	<0.001*	0.006*
Post-yield displace. (mm)	0.09 ± 0.1	0.66 ± 0.4	0.12 ± 0.1	0.38 ± 0.3	0.147	0.008*	0.071
Work-to-fracture (Nmm)	32.94 ± 5.02	9.39 ± 6.0	33.72 ± 4.6	8.54 ± 4.3	0.754	<0.001*	<0.001*
Elastic Modulus (N/mm^2)	6582.70 ± 1150.7	490.80 ± 303.1	5999.99 ± 1166.7	1170.71 ± 503.2	0.157	<0.001*	<0.001*

Ultimate Stress (N/mm^2)	152.07 ± 22.01	88.60 ± 41.4	153.46 ± 25.8	148.06 ± 31.7	0.002*	<0.001*	0.748
Yield Stress (N/mm^2)	121.60 ± 12.1	61.89 ± 31.7	130.64 ± 13.3	101.27 ± 29.0	0.032*	0.002*	0.040*

3.4. Interfragmentary strain influences the systemic immune response.

To comprehensively elucidate the local and systemic inflammatory responses to fracture and find predictive biomarkers of poor healing, we collected peripheral blood longitudinally from the high and low-strain groups at 1 and 24 hours, and days 3, 7, 14, and 21 post-fracture and callus tissue on day 21 post-fracture. Baseline values were collected five days prior to fracture induction. We employed multiplex assays and flow cytometry to analyze lymphoid (**Fig. 6A**) and myeloid cell (**Fig. 6B**) populations within the blood samples.

Our findings revealed rapid alterations in immune cell populations within the peripheral blood within one hour post-fracture in both groups (**Fig. 6**). Primarily, B-cell and monocyte/macrophage populations showed a sharp decrease in peripheral blood in both groups, likely due to the infiltration of these 'first responders' to the injury site. Moreover, the systemic immune response, concerning both total lymphoid (**Fig. 6A**(**i**)) and myeloid (**Fig. 6B**(**i**)) populations, exhibited significant differences between the groups on the first day post-fracture.

Intriguingly, the low-strain group demonstrated significantly lower B-cell percentages compared to the high-strain group (9.4% lower, *p=0.001*, **Fig. 6A**(**ii**)), while CD3+ T-cell population percentages were notably higher in the low-strain group compared to the high-strain group on day 1 (6.8% higher, *p=0.004*, **Fig. 6A**(**iii**)). Additionally, the CD4+ T-helper subpopulation, which was significantly lower in the low-strain group compared to the high-strain group one hour post-fracture (2.8% lower, p=0.032), exhibited a significant increase by day 1 (3% higher, *p=0.025*, **Fig. 6A**(**iv**)). Conversely, no significant changes were observed in cytotoxic T-cells (**Fig. 6A**(**v**)) or T-regulatory cells (**Fig. 6A**(**vi**)) post-fracture. Moreover, no other significant differences were observed on days 7, 14, and 21, including neutrophils (**Fig. 6B**(**ii**), monocytes (**Fig. 6B**(**iii**), and macrophage populations (**Fig. 6B**(**iv-vi**)).

Finally, an analysis of immune cells in the callus tissues on day 21 indicated that the total myeloid cell population in the low-strain group (52.9 ± 12.12%) was 14.3% higher than that in the high-strain fractures (38.57 ± 11.55%, *p=0.043*). However, no significant differences were observed in sub-populations. In summary, our data highlighted variations in the local and systemic inflammatory responses to fractures, dependent on the timing and strain conditions at the fracture site. Furthermore, general trends in cell populations suggested an early shift from innate to adaptive immunity in the low-strain group compared to the high-strain group.

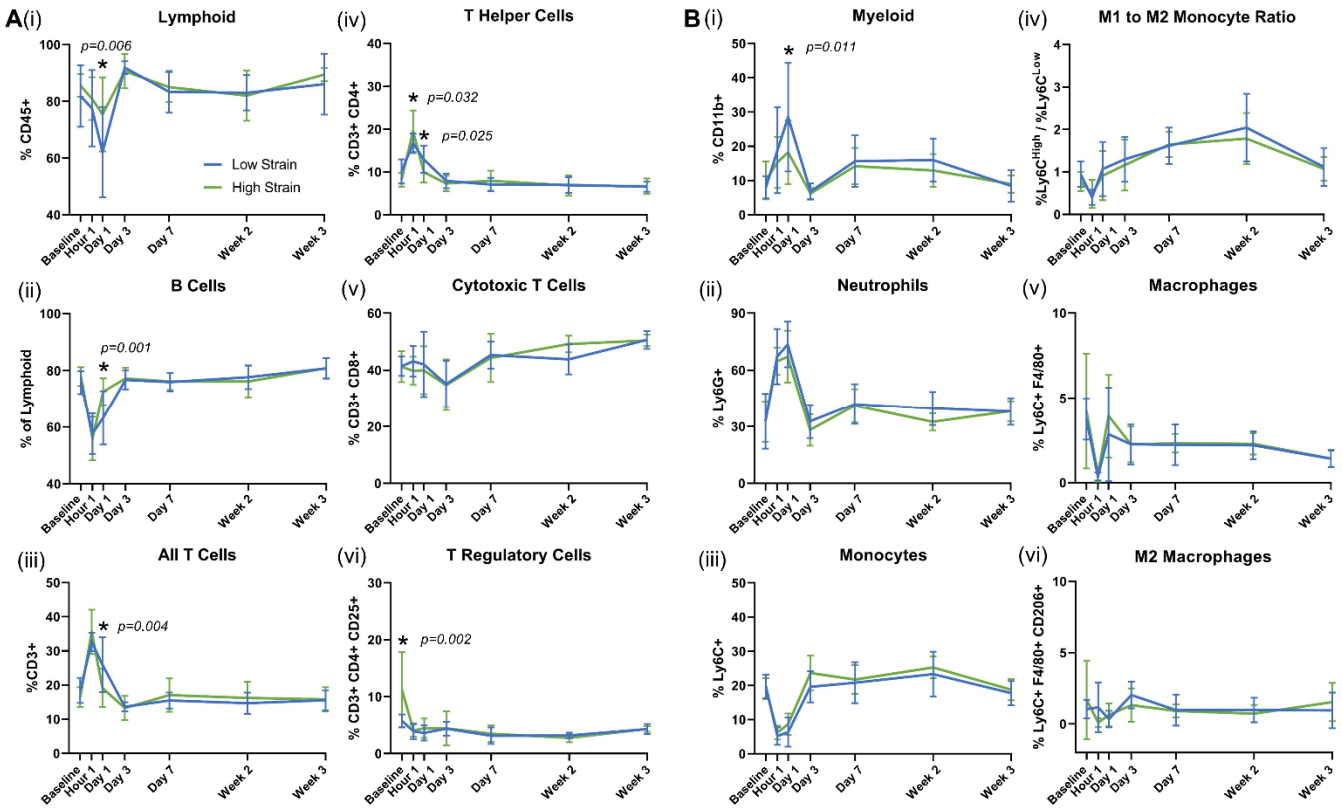

Figure 6. Temporal change in systemic lymphoid and myeloid cell populations post-fracture. A) *Lymphoid cell populations and subpopulations as percentages of parent populations at various time points.* ***B)*** *Myeloid cell populations and subpopulations as percentages of parent populations at various time points. n=7 for all groups. Baseline values were captured 5 days before fracture.*

3.5. Correlation of systemic and local immune factors correlate fracture healing outcomes.

Through thorough linear regression analysis, we identified 36 immune factors, including cell populations and cytokines/chemokines, that exhibited significant correlations with various functional healing outcomes (**Table 3).** Notably, some of these correlations clearly differentiated between the low and high-strain groups. For instance, the concentration of macrophage inflammatory protein-1 alpha (MIP-1α) on day 7 exhibited a robust positive correlation with both elastic modulus (R=0.970, *p=0.0013*) and stiffness (R=0.917, *p=0.009*). Another significant finding was the strong correlation between the concentration of leukemia inhibitory factor (LIF), a crucial bone anabolic factor, on day 3, and stiffness (R=0.986, p=0.014) and elastic modulus (R=0.970, p=0.030).

Furthermore, the neutrophil population on day 7 displayed significant correlations with maximum force (R=0.59, p=0.027) and ultimate stress (R=0.59, p=0.028). Notably, monocyte subsets in the callus on day 21 were significantly correlated with ultimate stress, with M1 monocytes exhibiting a negative correlation (R=-0.56, p=0.037) and M2 monocytes a positive correlation (R=0.59, p=0.037). CD4+ T cells in the day 21 callus also showed a negative correlation with stiffness (R=-0.57, p=0.034).

Interestingly, we observed intriguing trends related to T cells and their subpopulations (**Fig. 7**). For instance, on day 1 post-fracture, the total T cell population displayed a strong positive correlation with ultimate stress (R=0.71, *p=0.005*, **Fig. 7A**(**i**)). In contrast, the CD25+ T regulatory cell (Treg) population exhibited a strong negative correlation with ultimate stress (R=-0.59, p=0.026, **Fig. 7A**(**ii**)). On day 14, CD8+ T cells showed a strong negative correlation with ultimate stress (R=-0.62, p=0.017,

Fig. 7B(i)), while the CD25+ Treg cell population displayed a strong positive correlation with ultimate stress (R=0.58, p=0.030, **Fig. 7B**(**ii**)). These correlations highlight the significance of phenotype switches among innate and adaptive immune cells in the context of fracture healing.

Table 3. *Correlations between immune factors and healing outcomes*

Time Point	Biomarker	Healing Factor	R	p-value
Hour 1 *(Blood)*	CD25+ T cells	Ultimate stress (N/mm^2)	-0.562	0.036
	CD25+ T cells	Max Force (N)	-0.547	0.043
	CD8 T cells	Max Force (N)	0.544	0.044
	IL-6	Ultimate stress (N/mm^2)	-0.832	0.040
	MIG (CXCL9)	Max Force (N)	-0.810	0.051
Day 1 *(Blood)*	All T cells	Ultimate stress (N/mm^2)	0.707	0.005
	All T cells	Max Force (N)	0.670	0.001
	CD25+ T cells	Ultimate stress (N/mm^2)	-0.593	0.026
	DN T cells	Ultimate stress (N/mm^2)	-0.577	0.031
	B cells	Ultimate stress (N/mm^2)	-0.569	0.034
	Neutrophils	Ultimate stress (N/mm^2)	0.540	0.046
	Monocytes	Ultimate stress (N/mm^2)	-0.536	0.048
	Monocytes	Max Force (N)	-0.529	0.052
	CD25+ T cells	Max Force (N)	-0.525	0.055
	MIG (CXCL9)	Max Force (N)	-0.886	0.003
	IL-9	Max Force (N)	-0.756	0.030
	Eotaxin	Max Force (N)	-0.748	0.033
	IL-6	Max Force (N)	-0.714	0.047
Day 3 *(Blood)*	Neutrophils	Ultimate stress (N/mm^2)	0.549	0.042
	LIF	Stiffness (N/mm)	0.986	0.014
	LIF	Elastic Modulus (N/mm^2)	0.970	0.030
Day 7 *(Blood)*	Monocytes	Max Force (N)	-0.614	0.020
	Neutrophils	Max Force (N)	0.588	0.027
	Neutrophils	Ultimate stress (N/mm^2)	0.586	0.028
	Monocytes	Ultimate stress (N/mm^2)	-0.530	0.051
	MIP-1α	Elastic Modulus (N/mm^2)	0.970	0.001
	MIP-1α	Stiffness (N/mm)	0.917	0.010
	IL-1α	Max Force (N)	0.833	0.040
	MIG (CXCL9)	Ultimate stress (N/mm^2)	-0.719	0.045
	IL-1α	Stiffness (N/mm)	0.818	0.047
Day 14 *(Blood)*	CD8 T cells	Ultimate stress (N/mm^2)	-0.628	0.017
	CD25+ T cells	Ultimate stress (N/mm^2)	0.579	0.030
Day 21 *(Blood)*	Myeloid	Stiffness (N/mm)	-0.560	0.038
Day 21 *(Callus)*	CD4 T cells	Stiffness (N/mm)	-0.566	0.035
	M1 Mono	Ultimate stress (N/mm^2)	-0.559	0.038
	M2 Mono	Ultimate stress (N/mm^2)	0.559	0.038

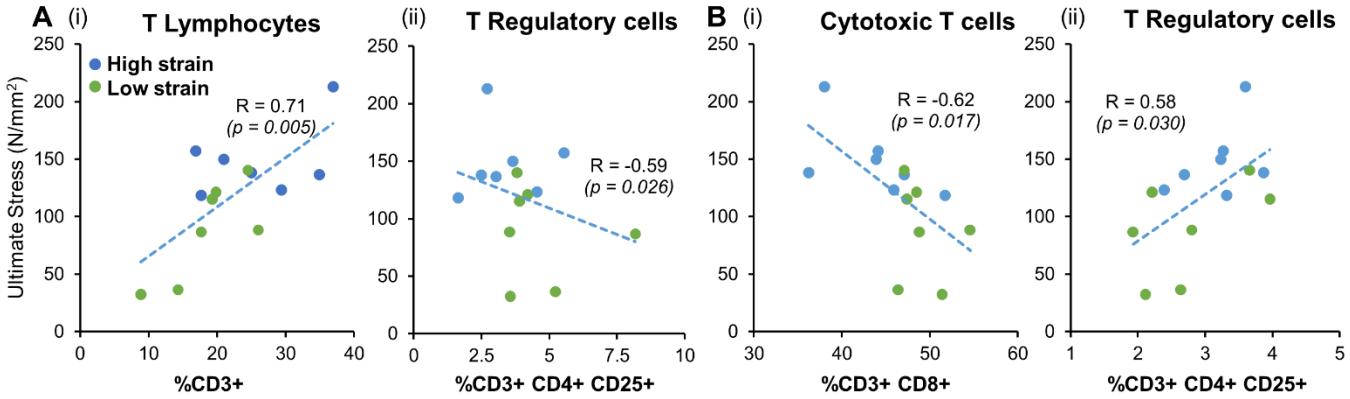

Figure 7. Correlations between systemic T cell populations and ultimate stress at day 21. A) *Day 1: (i) Linear correlation plot between the percentage of all CD3+ T cells and ultimate stress. (ii) Linear correlation plot between the percentage of CD25+ regulatory T cells and ultimate stress.* ***B)*** *Day 14: (i) Linear correlation plot between the percentage of CD8+ cytotoxic T cells and ultimate stress. (ii) Linear correlation plot between the percentage of CD25+ regulatory T cells and ultimate stress.*

3.6. Identification of immune phenotypes as predictors of functional healing

To identify the immune phenotypes that serve as the most accurate predictors of functional healing, we employed a partial least squares regression (PLSR) algorithm. This method allowed us to assess the collective influence of immune cell populations at various time points (1 hour and days 1, 3, 7, 14, and 21) on healing outcomes at day 21. For our healing outcomes, we considered whole-bone properties (stiffness and maximum force) and tissue-level properties (ultimate stress and elastic modulus), following established[26]. The PLSR algorithm calculated weighted averages for all analyzed immune cell populations in the peripheral blood (X score) and plotted them against weighted functional healing outcomes (Y score). We observed significant correlations with maximum separation between the low and high-strain groups at three specific time points: 1 hour (R=0.71, p=0.005), day 3 (R=0.57, p=0.032), and day 7 (R=0.72, p=0.004) (**Fig. 8**).

Our analysis focused on identifying the immune cell populations that were most influential in predicting healing outcomes. Notably, we found that macrophage populations exhibited the strongest predictive power at all three time points. Specifically, the CD206+ macrophage subpopulation at 1 hour (weighted coefficient = 0.228) and the total F4/80+ macrophage population at day 3 (weighted coefficient = 0.206) demonstrated the best predictive capacity. On day 14, our analysis revealed that the CD25+ regulatory T cells (weighted coefficient = 0.958) and CD206+ macrophages (weighted coefficient = 0.233) were the most reliable predictors of the day 21 healing outcomes.

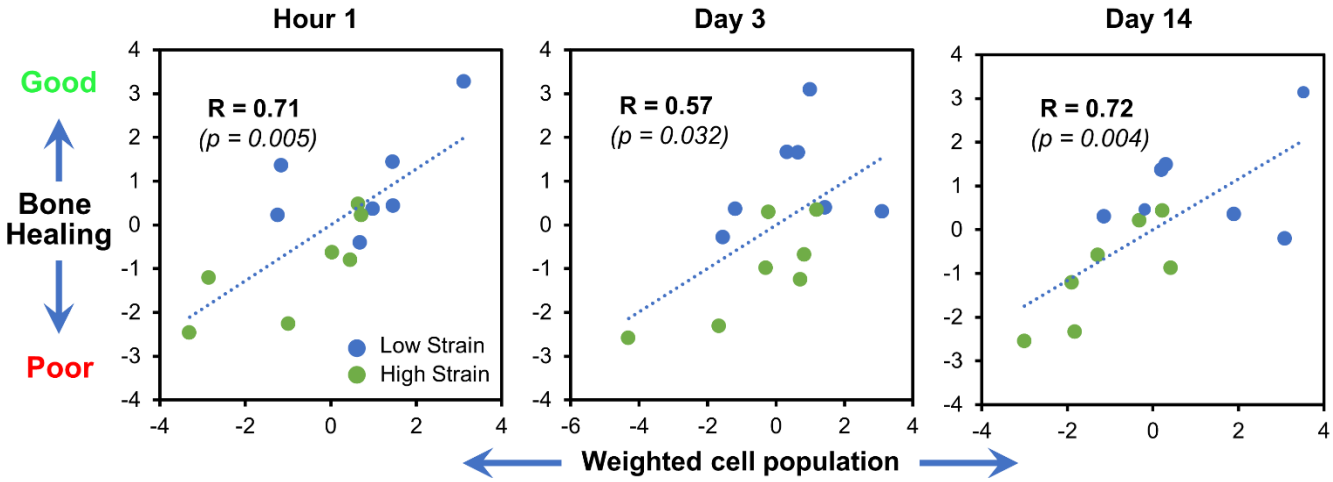

Figure 8. Multivariate analysis of immune cell populations with healing outcomes. *This PLSR plot displays the weighted averages for all analyzed systemic immune cell populations in the peripheral blood (X score) at 1 hour and days 3 and 14 against weighted functional healing outcomes (Y score). The chosen healing outcomes are represented by whole-bone properties (stiffness and maximum force) and tissue-level properties (ultimate stress and elastic modulus).*

4. Discussion

Hypertrophic nonunions present a significant challenge in patient care due to the difficulty in achieving a timely diagnosis. Improving diagnostic times and treatment options necessitates a more comprehensive understanding of nonunion pathology. However, current animal models of nonunion only reproduce the etiology of atrophic nonunion, which are diagnosed relatively earlier, or use delayed healing models by withholding treatment after creating a segmental defect for an extended period[21], which does not mirror the clinical standard of care. But predominant cases of nonunion in the clinic are due to a lack of proper stability, referred to as hypertrophic nonunion. Therefore, we developed a model that mirrors the standard of care in the clinic while delaying the healing outcomes by destabilizing the defect, as seen in hypertrophic nonunion.

Mechanical signals are the key regulators of bone homeostasis. The mechanotransduction process is not only critical for bone remodeling but also guides the fracture healing cascade. The mechanical disruption at the organ level in fracture results in a mechanical response at tissue, cellular, and molecular levels. Interfragmentary strain is the most representative measure of fracture stability. At a tissue level, the interfragmentary strains are central in determining the inflammatory response, vascularization, osteogenesis, and osteoclastogenesis[28]. A disruption of the tissue-level mechanical signals results in fibrosis and nonunion of the fracture. We aim to improve clinical care for recalcitrant fractures by elucidating the underlying mechanopathology, identifying predictive biomarkers, and engineering methods to reduce this burden in patients.

4.1. A murine model of hypertrophic nonunion and delayed healing

The stiffness of the fixation construct is the principal determinant of the interfragmentary strains, thereby influencing the mechanism and progression of healing[29]. Hence, to study and evaluate the cellular level response locally and systemically, we modified the fracture mechanics by engineering intramedullary (IM) nails with varying stiffness. We chose nitinol alloy for the IM nails due to its high strength and superelastic strain recovery[30], and they exhibit no cytotoxicity, genotoxicity, or allergic activity. In addition, they have lower elastic modulus than traditional implant metals and hence can reduce stress shielding. Their ability for sustained application of forces due to their pseudoelasticity is

mechanobiologically favored for fracture fixation[31]. We created a library of IM nails with varying stiffnesses and chose the ones that create interfragmentary strains projected to cause maximum and minimum levels of ossification of the callus (i.e., 5-15% strain). In both groups, we saw symmetrical callus formation. However, as expected, higher flexure strains (>15%) induced by low-stiffness nails resulted in significantly larger callus volume and poorer functional healing outcomes than the lower strain group (<5%). Our observations are consistent with clinical data showing that reduced interfragmentary strain using stiffer constructs often reduces callus volume[32]. The callus volume is usually influential and correlates positively with healing when the segments are not in close proximity, as demonstrated in segmental defect models[33, 34]. However, in our model, the bone segments are in close proximity in both groups, and the high strain induced a larger callus volume, yet they resulted in poorer healing outcomes. The two groups had no significant differences in the callus BV/TV or callus BMD. Therefore, the higher interfragmentary strain allowed by the low-stiffness nails is too high to support callus ossification and healing. Hence, our model recreates a similar pathological scenario seen in the clinical cases enabling us to investigate the underlying mechanism.

One limitation of our study is the inability to continuously monitor strain at the fracture site over time and establish direct associations with the immune response. Nevertheless, our findings align with in-silico models that predict impaired healing and the development of fibrosis under conditions of higher initial strain[34]. In our future research, we will prioritize the implementation of longitudinal measurements of local strain to establish a more comprehensive association with the immune response.

4.2. Translational shear and fibrosis in hypertrophic nonunion

The magnitude and the direction of interfragmentary strain and shear is critical in determining the outcome of secondary fracture healing[35]. Fracture strain at early time points, generally stimulates callus formation[36], but the ultimate healing outcomes are more dependent on strain type and magnitude. Axial compression can promote larger callus formation and cartilaginous bridging that can stabilize the fracture[37], while translational shear at comparable magnitude are detrimental to the healing[38]. In-silico models show that the translational shear impedes with healing processes the most, while the tortional shear has marginal effects[35]. Likewise higher strain rates, in all three loading conditions lead to compromised healing[35].

Our delayed-healing model allowed more translational shear in the high-strain groups due to the hyperflexibility of IM rods, while permitting a similar unconstrained level of tortional shear and axial compression between groups. Further, to harness the benefits of reamed-intramedullary nailing shown in closed fractures[39], we reamed with gauge sizes that appropriately fit the low and high stiffness IM nails.

In our experimental model, we observed larger calluses in the high-strain groups, while the low-strain groups exhibited smaller callus sizes and early endochondral ossification by the third week. Notably, the high-strain groups exhibited late-stage callus fibrosis, characterized by atypical fibrillar collagen deposition, a hallmark of delayed healing factures[40]. Consequently, the cartilaginous bridging of the fracture gap and subsequent bone formation and healing were significantly delayed. Our delayed-healing model effectively recapitulated the pathogenesis of hypertrophic nonunions by faithfully replicating the biomechanical aspects of the fracture. Importantly, our findings challenge conventional wisdom by demonstrating that elevated stiffness ranges contribute to improved healing, in contrast to the notion of impaired healing in murine models. It is worth noting that further exploration of upper stiffness limits remains a topic for future investigation.

4.3. Immune dysfunction and biomarkers to predict functional healing.

Understanding the dynamics of immune cell recruitment and stromal cell differentiation within the fracture site is crucial for identifying potential therapeutic targets and predictive markers of impaired healing. Furthermore, the role of systemic and local immune dysregulation in delayed fracture healing remains to be fully elucidated. To address this knowledge gap, we conducted a comprehensive analysis of immune cells and factors in both normal and delayed-healing fractures and correlated these findings with healing outcomes. The process of fracture healing traditionally consists of four phases: (i) inflammation, (ii) soft callus (cartilaginous) formation, (iii) hard callus (bony) formation, and (iv) remodeling. Our observations revealed that, in both groups, the inflammatory phase commenced within minutes of fracture induction. Notably, significant differences in terms of systemic immune cell populations were evident at 1 hour and 24 hours post-fracture between the groups. However, no significant alterations were observed after day 3, underscoring the need for a more in-depth investigation. It is essential to recognize that many immune cells and factors exert redundant and pleiotropic effects, making simple comparative analyses insufficient to unveil complex relationships. Consequently, we conducted both univariate and multivariate analyses to gain deeper insights into these correlations.

Univariate analyses have revealed positive associations between long-term healing outcomes and systemic immune cell populations, including monocytes, neutrophils, and T-cells. These favorable correlations were also evident with specific myeloid cell recruitment factors, namely MIP-1α and IL-1α[41], along with the bone anabolic cytokine LIF[42], particularly at the early time points (ranging from 1 hour to Day 7 post-fracture). Conversely, negative correlations were noted between systemic myeloid and CD8+ T cell populations at later time points (Day 14-21) and healing. Interestingly, CD25+ T regulatory cells demonstrated a positive correlation with healing at these later time points. These findings lend support to the notion that a timely transition from proinflammatory signals in the early stages to pro-regenerative signals plays a pivotal role in fracture healing, consistent with previous reports[43]. Additionally, these results suggest that delayed healing in our model is associated with an increase in systemic CD8+ T cell populations, which coincides with a reduction in systemic and local callus CD25+ T-regulatory cells. Collectively, our data corroborates our initial hypothesis that delayed healing is linked to systemic and local immune dysregulation.

It is essential to note that our analysis of peripheral blood samples unveiled dynamic fluctuations in adaptive immune cell populations, both at early and late time points. Traditionally, these adaptive cell populations have not been the primary focus of wound healing studies. However, recent research has emphasized the crucial role of adaptive cell populations in healthy fracture healing. These cells influence the fracture healing process by contributing to either osteoclast or osteoblast differentiation[44]. Early osteoclastogenesis is vital following a fracture to clear debris and create a conducive environment for healing. However, a subsequent shift toward osteoblast activity is essential to generate new woven bone and gradually stabilize the fracture site.

Next, we performed an in-depth analysis of cell populations using multivariate PLSR algorithm to predict functional bone healing. The results underscore the significant influence of systemic CD25+ T-regulatory cells as predictive biomarkers for healing. Additionally, CD206+ macrophage populations emerged as the next influential cell populations in predicting successful fracture healing. Hence, our findings suggest that the timely resolution of inflammatory signals post-trauma and the elevation of pro-regenerative immune cell phenotypes are essential for bone regeneration, and a deficiency in these processes contributes to delayed healing.

5. Summary and Conclusion

The ability to predict the quality of fracture healing early represents a valuable clinical asset for diagnosing nonunion. Presently, a "wait and watch" strategy is employed to diagnose nonunion, which leaves patients suffering until surgical intervention is considered necessary, at an average duration of 8

months[4]. The potential exists to significantly reduce this timeframe by developing univariate and multivariate models capable of rapidly predicting healing based solely on peripheral cell populations. Our studies identified CD8+ cytotoxic T cells and CD25+ T-regulatory cells as critical negative and positive correlates, respectively, among lymphoid cells for normal bone healing. Furthermore, systemic macrophage populations, along with late CD206+ populations, were associated with improved healing outcomes. Nevertheless, further mechanistic investigations are warranted to validate their roles in either delaying or promoting bone regeneration. Notably, our studies offer valuable insights into the interplay between interfragmentary strain and the inflammatory response and highlight the association between systemic immune health and bone regeneration. These findings provide a strong foundation for future research aimed at developing immunomodulatory strategies to address immune dysfunction and enhance bone regeneration as well as understanding, treating, preventing nonunion from a mechanico-surgical perspective.

In summary, we have successfully developed a murine delayed-healing model that faithfully replicates the etiology of hypertrophic nonunion by recreating the mechanical environment of the fracture site. Our delayed healing fracture model not only offers valuable insights into the persistent clinical problem of fracture nonunion but also provides a clinically representative platform for investigating the complexities behind nonunion development. Of particular note, this model challenges the prevailing belief by demonstrating that higher stiffness levels contribute to better, rather than poorer, healing in a murine context. Nonetheless, further investigations are needed to determine the upper limits of stiffness in this context. A comprehensive understanding of nonunion pathology will pave the way for the advancement of novel diagnostic and treatment strategies, ultimately bringing us closer to the eradication of this issue.

6. Supplementary Materials

Supplementary Table1:

Target	Conjugate	Clone	Supplier	Antibody Dilution
CD45	BV 605	30-F11	BioLegend	1:800
CD11b	APC-Cy7	M1/70	BD Biosciences	1:200
CD11c	BUV 496	HL3	BD Biosciences	1:200
Ly-6G	PE	1A8	BioLegend	1:200
Ly-6C	PE-Cy7	HK1.4	ThermoFisher	1:200
F4/80	BV 421	BM8	BioLegend	1:200
CD206	AF 647	MR5D3	Bio-Rad	1:200
CD3	AF 700	17A2	ThermoFisher	1:200
CD8	BV 711	53-6.7	BD Biosciences	1:200
CD4	BV 650	RM4-5	BioLegend	1:200
CD25	FITC	7D4	BD Biosciences	1:100
CD19	BV480	1D3	BD Biosciences	1:200
CD16/32	Unconjugated	93	ThermoFisher	4 µg / 2 million cells

Supplementary Table 2:

	Cell Types	**Surface Markers**
Myeloid (CD45+ CD11b+)	Monocytes (M1)	$F4/80^{-}$ $Ly6G^{-}$ $Ly6C^{Hi}$
	Monoctyes (M2)	$F4/80^{-}$ $Ly6G^{-}$ $Ly6C^{Lo}$
	Macrophage (M1)	$F4/80^{+}$ $Ly6G^{-}$ Ly6CHi
	Macrophage (M2)	$F4/80^{+}$ $Ly6G^{-}$ CD206
	Dendritic cells	$Ly6G^{-}$ $CD11c^{+}$
	Neutrophils	$Ly6G^{+}$
Lymphoid (CD45+ CD11b-)	T cells (Cytotoxic)	$CD3^{+}$ $CD8^{+}$
	T cells (Helper)	$CD3^{+}$ $CD4^{+}$
	T cells (Treg)	$CD3^{+}$ $CD4^{+}$ $CD25^{+}$
	B cells	$CD19^{+}$

7. Acknowledgements

Research reported in this publication was supported in part by the National Institute of Arthritis and Musculoskeletal and Skin Diseases (NIAMS) Award Number R21AR078447, National Institute of General Medical Sciences (NIGMS) of the National Institutes of Health under Award Number P20GM130456, Orthopedic Trauma Association (OTA, Grant Number: 6889), and Biospecimen Procurement & Translational Pathology Shared Resource Facility of the University of Kentucky Markey Cancer Center Award Number P30CA177558. The content is solely the responsibility of the authors and does not necessarily represent the official views of the National Institutes of Health or other grant funding agencies.

8. Reference

1. Holmes, D. Closing the gap. *Nature* **550**, S194-S195 (2017).
2. Schottel, P.C., O'Connor, D.P. & Brinker, M.R. Time trade-off as a measure of health-related quality of life: long bone nonunions have a devastating impact. *The Journal of Bone and Joint Surgery. American Volume* **97**, 1406 (2015).
3. Wildemann, B. et al. Non-union bone fractures. *Nature Reviews Disease Primers* **7**, 1-21 (2021).
4. Ekegren, C.L., Edwards, E.R., De Steiger, R. & Gabbe, B.J. Incidence, costs and predictors of non-union, delayed union and mal-union following long bone fracture. *International journal of environmental research and public health* **15**, 2845 (2018).
5. Cunningham, B.P., Brazina, S., Morshed, S. & Miclau III, T. Fracture healing: A review of clinical, imaging and laboratory diagnostic options. *Injury* **48**, S69-S75 (2017).
6. Weber, B.G. & Cech, O. in Pseudarthrosis: pathophysiology, biomechanics, therapy, results 323-323 (1976).
7. Andrzejowski, P. & Giannoudis, P.V. The 'diamond concept'for long bone non-union management. *Journal of Orthopaedics and Traumatology* **20**, 1-13 (2019).
8. Elliott, D. et al. A unified theory of bone healing and nonunion: BHN theory. *The bone & joint journal* **98**, 884-891 (2016).
9. Rupp, M. et al. Do systemic factors influence the fate of nonunions to become atrophic? A retrospective analysis of 162 cases. *BioMed Research International* **2019** (2019).
10. Wolff, J. The law of bone remodelling. (Springer Science & Business Media, 2012).
11. FROST, H. 'Mass' and the 'mechanostat': a proposal. *Anat. Rec.* **219**, 1-9 (1987).
12. Perren, S. Physical and biological aspects of fracture healing with special reference to internal fixation. *Clinical orthopaedics and related research*, 175-196 (1979).
13. Claes, L. & Heigele, C. Magnitudes of local stress and strain along bony surfaces predict the course and type of fracture healing. *Journal of biomechanics* **32**, 255-266 (1999).
14. Loi, F. et al. Inflammation, fracture and bone repair. *Bone* **86**, 119-130 (2016).
15. Bastian, O.W. et al. Impaired bone healing in multitrauma patients is associated with altered leukocyte kinetics after major trauma. *J Inflamm Res* **9**, 69-78 (2016).
16. Reinke, S. et al. Terminally differentiated $CD8^+$ T cells negatively affect bone regeneration in humans. *Sci Transl Med* **5**, 177ra136 (2013).
17. Dishowitz, M.I. et al. Systemic inhibition of canonical Notch signaling results in sustained callus inflammation and alters multiple phases of fracture healing. *PloS one* **8**, e68726 (2013).
18. Hebb, J.H. et al. Bone healing in an aged murine fracture model is characterized by sustained callus inflammation and decreased cell proliferation. *Journal of orthopaedic research : official publication of the Orthopaedic Research Society* **36**, 149-158 (2018).
19. Zondervan, R.L., Vorce, M., Servadio, N. & Hankenson, K.D. Fracture Apparatus Design and Protocol Optimization for Closed-stabilized Fractures in Rodents. *Journal of visualized experiments : JoVE* (2018).
20. Bonnarens, F. & Einhorn, T.A. Production of a standard closed fracture in laboratory animal bone. *Journal of orthopaedic research : official publication of the Orthopaedic Research Society* **2**, 97-101 (1984).

21. Zhu, W. et al. Ankylosing spondylitis: etiology, pathogenesis, and treatments. *Bone Research* **7**, 22 (2019).
22. Lybrand, K., Bragdon, B. & Gerstenfeld, L. Mouse Models of Bone Healing: Fracture, Marrow Ablation, and Distraction Osteogenesis. *Current Protocols in Mouse Biology* **5**, 35-49 (2015).
23. Histing, T. et al. Small animal bone healing models: standards, tips, and pitfalls results of a consensus meeting. *Bone* **49**, 591-599 (2011).
24. Bartnikowski, M., Bartnikowski, N., Woloszyk, A., Matthys, R. & Glatt, V. Genetic variation in mice affects closed femoral fracture pattern outcomes. *Injury* **50**, 639-647 (2019).
25. Patrick, M.D., Keys, J.F., Suresh Kumar, H. & Annamalai, R.T. Injectable nanoporous microgels generate vascularized constructs and support bone regeneration in critical-sized defects. *Scientific Reports* **12**, 15811 (2022).
26. Jepsen, K.J., Silva, M.J., Vashishth, D., Guo, X.E. & van der Meulen, M.C.H. Establishing Biomechanical Mechanisms in Mouse Models: Practical Guidelines for Systematically Evaluating Phenotypic Changes in the Diaphyses of Long Bones. *Journal of Bone and Mineral Research* **30**, 951-966 (2015).
27. Wildemann, B. et al. Non-union bone fractures. *Nat Rev Dis Primers* **7**, 57 (2021).
28. Augat, P., Hollensteiner, M. & von Ruden, C. The role of mechanical stimulation in the enhancement of bone healing. *Injury* **52 Suppl 2**, S78-S83 (2021).
29. Claes, L.E. et al. Effects of mechanical factors on the fracture healing process. *Clinical orthopaedics and related research*, S132-147 (1998).
30. Bansiddhi, A., Sargeant, T.D., Stupp, S.I. & Dunand, D.C. Porous NiTi for bone implants: a review. *Acta Biomater* **4**, 773-782 (2008).
31. Safranski, D., Dupont, K. & Gall, K. Pseudoelastic NiTiNOL in Orthopaedic Applications. *Shape Memory and Superelasticity* **6**, 332-341 (2020).
32. Bottlang, M. et al. Effects of construct stiffness on healing of fractures stabilized with locking plates. *The Journal of bone and joint surgery. American volume* **92 Suppl 2**, 12-22 (2010).
33. Bottlang, M. & Feist, F. Biomechanics of Far Cortical Locking. *Journal of Orthopaedic Trauma* **25** (2011).
34. Ghiasi, M.S., Chen, J.E., Rodriguez, E.K., Vaziri, A. & Nazarian, A. Computational modeling of human bone fracture healing affected by different conditions of initial healing stage. *BMC Musculoskeletal Disorders* **20**, 562 (2019).
35. Steiner, M., Claes, L., Ignatius, A., Simon, U. & Wehner, T. Disadvantages of interfragmentary shear on fracture healing--mechanical insights through numerical simulation. *Journal of orthopaedic research : official publication of the Orthopaedic Research Society* **32**, 865-872 (2014).
36. Barcik, J. et al. The absence of immediate stimulation delays bone healing. *Bone* **175**, 116834 (2023).
37. Windolf, M., Ernst, M., Schwyn, R., Arens, D. & Zeiter, S. The relation between fracture activity and bone healing with special reference to the early healing phase - A preclinical study. *Injury* **52**, 71-77 (2021).
38. Augat, P. et al. Shear movement at the fracture site delays healing in a diaphyseal fracture model. *Journal of Orthopaedic Research* **21**, 1011-1017 (2003).
39. Bhandari, M. et al. Randomized trial of reamed and unreamed intramedullary nailing of tibial shaft fractures. *The Journal of bone and joint surgery. American volume* **90**, 2567-2578 (2008).

40. Khajuria, D.K. et al. Aberrant structure of fibrillar collagen and elevated levels of advanced glycation end products typify delayed fracture healing in the diet-induced obesity mouse model. *Bone* **137**, 115436 (2020).
41. Baht, G.S., Vi, L. & Alman, B.A. The Role of the Immune Cells in Fracture Healing. *Curr Osteoporos Rep* **16**, 138-145 (2018).
42. Nicola, N.A. & Babon, J.J. Leukemia inhibitory factor (LIF). *Cytokine & growth factor reviews* **26**, 533-544 (2015).
43. Newman, H., Shih, Y.V. & Varghese, S. Resolution of inflammation in bone regeneration: From understandings to therapeutic applications. *Biomaterials* **277**, 121114 (2021).
44. Könnecke, I. et al. T and B cells participate in bone repair by infiltrating the fracture callus in a two-wave fashion. *Bone* **64**, 155-165 (2014).